# Fatigue Crack Growth and Life Prediction of 7075-T62 Aluminium-alloy Thin-sheets with Low-velocity Impact Damage under Block Spectrum Loading

**Zheng-Qiang Cheng[a,b], Jun-Jiang Xiong[a], Wei Tan[b,*]**

[a] School of Transportation Science and Engineering, Beihang University, Beijing 100191, People's Republic of China

[b] School of Engineering and Materials Science, Queen Mary University of London, London E1 4NS, United Kingdom (* Corresponding author. E-mail address: wei.tan@qmul.ac.uk)

**Abstract:** This paper developed a fatigue crack growth model considering the effects of load interaction and low-velocity impact (LVI) damage. Fatigue crack growth (FCG) accumulative method was established to assess crack growth life of aluminium-alloy thin-sheets with LVI damage under spectrum loading. To validate the proposed model, LVI tests of 7075-T62 aluminium-alloy thin-sheets were conducted, followed by post-impact constant amplitude tension-tension and block spectrum loading FCG tests. Experimental results indicate that there are two competing mechanisms for the effect of LVI damage on the subsequent FCG behaviour of aluminium-alloy thin-sheets. One is the retardation effect on the crack growth rate from the dented plastic zone caused by LVI, and the other is the acceleration effect from the stress concentration due to impact-induced geometric changes. The new FCG model achieves a good agreement with FCG results of post-impact aluminium-alloy thin-sheets and can capture the LVI damage effect, opening an avenue to predict FCG life of aluminium-alloy thin-sheets with LVI damage.

**Keywords: Low velocity impact, aluminium-alloy thin-sheets, fatigue crack growth, life prediction, block spectrum loading.**

## 1. Introduction

Aeronautic aluminium-alloy thin-sheets are the primary structural material for aircraft skins. During aircraft take-off, landing and maintenance, aircraft skins are inevitably and occasionally encounter low-velocity impact (LVI) events from foreign objects, such as flying runway gravel, accidental tool drop, and collision with ground vehicles [1]. LVI dents, as a typical damage type of aircraft skins, are one of the main reasons that affect the ultimate strength and fatigue life of aircraft structures [2]. At present, reliable evaluation for the LVI damage tolerance performance of aircraft remains a challenge to the aviation industry [3].

The effects of impact dent shape (such as spherical, conical, elliptical, V-shape, and U-shape) [4,5], impact-induced global deflection [4,5], dent depth [6] and dent repairing [7] on the post-impact static behaviours of aluminium-alloy thin-sheets have been widely investigated. It has been reported that

impact-induced global deflection dominates the ultimate compressive strength of 2024-T3 aluminium-alloy thin-sheets with LVI damage, however, local dent depth dominates its ultimate tensile strength and the ultimate tensile strength decreases with the increase of indentation depth. The indenter shape significantly affects the declining trend of ultimate tensile strength [4,5]. Inconsistently, as for the 2024-T3 aluminium-alloy stiffened plate, medium dents can increase its ultimate compressive strength while shallow or deep dents will reduce its ultimate compressive strength [6]. Compared to undamaged materials, the yield strength and ultimate tensile strength of dent-repaired 2024-T3 aluminium-alloy thin-sheets are slightly increased, while the elongation is slightly reduced [7].

Moreover, a large number of researchers have studied the effects of indenter shape (such as spherical, conical, and U-shape) [8,9], dent depth [2,8-10], impactor diameter [9], impact modes (such as a single impact, continuous twice-impacts at the same position and impacts at two parallel positions) [10], coupled damage with impact and pre-fatigue [11], dent repairing (such as rotary peening [7], quasi-static compression of the dent [11] and hammer manual reworking [12,13]) on the post-impact fatigue behaviours of aluminium-alloy thin-sheets. It has been revealed that conical dent damage leads to the greatest reduction in the fatigue life of 2024-T3 aluminium-alloy thin-sheets under constant amplitude tension-tension fatigue loads, followed by the U-shape dent damage, and then spherical dent damage [8,9]. Impact dents will significantly reduce the fatigue life of 2024-T3, 2524-T3 and 7075-T62 aluminium-alloy thin-sheets, and their fatigue life gradually decrease with the increase of indentation depth [2,8-10]. At the same indentation depth, the fatigue life of the aluminium-alloy thin-sheets gradually decreases with the increasing impactor diameter [9]. With the increase of the dent damage volume caused by the aforementioned three impact modes, the fatigue life of 2198-T8 aluminium-lithium alloy thin-sheets gradually decreases [10]. Dent repairing promotes the redistribution of the strain field on the surface of the specimen and effectively reduces the uneven distribution of residual strain and stress concentration caused by LVI, so it delays the initiation of micro-cracks at the dent edge area and can effectively restore the fatigue life of the aluminium-alloy thin-sheets [11-13]. However, the recovery extent of fatigue life is related to the fatigue stress level. Dent repairing can bring the fatigue life back to its original level at the lower fatigue stress, but it does not improve the fatigue life at the higher fatigue stress [7]. For pre-fatigue specimens with micro-cracks, dent repairing could not restore fatigue life but will magnify the micro-cracks caused by pre-fatigue damage due to impact and repair, further reducing the fatigue life of aluminium-alloy thin-sheets [11].

The aforementioned literatures prove that the effect of LVI damage on the static strength and fatigue life of aeronautic aluminium-alloy thin-sheets has been studied systematically. In fact, LVI loading

not only leads to geometric changes of aluminium-alloy thin-sheets, but also cause permanent plastic zone, and both phenomena significantly affect the fatigue crack growth (FCG) behaviours. However, research on this problem is very scarce, and the LVI damage effect on the FCG behaviours of aluminium-alloy thin-sheets remains unaddressed. So far, only a few experimental studies have obtained incomplete research results [8,12-14]. Li et al. [8] experimentally studied the effect of spherical, conical and U-shape impact dent damage on the FCG behaviours of 2024-T3 aluminium-alloy thin-sheets. The results demonstrate that conical dent damage shortens FCG life while spherical and U-shape dent damage prolong FCG life. Shivalli and Smith [13,14] conducted constant-amplitude tension-tension FCG tests for 2024-T3 aluminium-alloy thin-sheets with LVI damage. It has been illustrated that the overall FCG rate of post-impact specimens is significantly greater than that of undamaged specimens, so the FCG life of the specimens with LVI damage is considerably shorter than that of undamaged specimens. Hence, it can be seen that the mechanism of LVI damage on the FCG behaviours of aeronautic aluminium-alloy thin-sheets is not clear. In addition, the quantitative characterisation model has not been established, and the FCG life prediction methodology of aluminium-alloy thin-sheets with LVI damage under spectrum loading has not been reported. In engineering practice, the fatigue crack often originates from the position of the rivet which is used to connect the skins to the frame due to stress concentration. The fatigue origins are usually away from the dent on the aircraft skins caused by the inevitable LVI events. Under this circumstance, the effect of a dent on crack growth path and life for aircraft skins are the main practical concerns for engineers. Therefore, it is essential to systematically investigate the FCG behaviours of aeronautic aluminium-alloy thin-sheets with LVI damage, and develop a quantitative FCG characterisation model and life prediction approach for post-impact structures, providing technical support for engineering design.

The main novel contributions of this paper herein are: **(i)** For the first time in the literature, constant amplitude FCG tests at different stress ratios and block spectrum loading were performed on 7075-T62 aluminium-alloy thin-sheets with LVI damage. **(ii)** A new FCG model considering the effects of load interaction and LVI damage was proposed, and the accumulative methodology of FCG life was established to assess crack growth life of post-impact aluminium-alloy thin-sheets under spectrum loading. **(iii)** Mechanisms of LVI damage on sequent FCG behaviours of aluminium-alloy thin-sheets were revealed. Our theoretical model and test results can provide guidelines for the impact damage tolerance design of aeronautic aluminium-alloy structures.

## 2. FCG model and life prediction method considering the effects of load interaction and LVI damage

An empirical FCG model based on previous contribution [15] is proposed to depict the near-threshold region and the stable or linear crack growth rate region by accounting for the effects of stress ratio

and crack growth threshold:

$$\frac{da}{dN}=\begin{cases}C\left(\Delta K-\Delta K_{\text{th}}\right)^{m_1}\left(1-R\right)^{m_2}, \Delta K \geq \Delta K_{\text{th}} \\ 0 \qquad\qquad\qquad\qquad\quad , \Delta K < \Delta K_{\text{th}}\end{cases} \tag{1}$$

where $da/dN$ is the crack growth rate; $R$ is the stress ratio; $\Delta K$ and $\Delta K_{\text{th}}$ are the stress intensity factor range and crack growth threshold, respectively; $C$, $m_1$ and $m_2$ are the material constants in FCG model and are determined from the constant amplitude FCG test data by the Least Squares Fitting method (see Appendix A). Obviously, Eq. (1) is a $da/dN$-$\Delta K$-$R$ surface equation to depict the relationship between FCG rate, stress intensity factor range and stress ratio.

In fact, aircraft structures often suffer from random fatigue spectrum loading during flight. The load interaction in the random fatigue spectrum loading has a significant effect on the crack growth behaviours, which is mainly manifested as tensile overload retardation effect, compressive load acceleration effect, and the reduction of overload retardation effect caused by the compressive load immediately following the tensile overload. So far, many models have been used to characterise the load interaction effect [15-17]. Based on Eq. (1), the FCG model considering load interaction effect can be expressed as

$$\frac{da}{dN}=\begin{cases}C\left(\Delta K-\Delta K_{\text{th}}\right)^{m_1}\left(1-R_{\text{eff}}\right)^{m_2} , \Delta K \geq \Delta K_{\text{th}} \\ 0 \qquad\qquad\qquad\qquad\quad , \Delta K < \Delta K_{\text{th}}\end{cases} \tag{2}$$

and

$$R_{\text{eff}}=1-\frac{\Delta K}{\left(K_{\max}\right)_{\text{eff}}} \tag{3a}$$

$$\left(K_{\max}\right)_{\text{eff}}=K_{\max}-\frac{\left(K_{\max}\right)_{\text{OL}}-\left(K_{\max}\right)_{\text{th}}}{\left(r_{\text{so}}-1\right)\left(K_{\max}\right)_{\text{OL}}}\left(\left(K_{\max}\right)_{\text{OL}}\sqrt{1-\frac{\Delta a'}{Z_{\text{OL}}}}-K_{\max}\right) \tag{3b}$$

$$\left(K_{\max}\right)_{\text{th}}=\frac{\Delta K_{\text{th}}}{\left(1-R\right)} \tag{3c}$$

$$Z_{\text{OL}}=\frac{1}{2\pi}\left(\frac{\left(K_{\max}\right)_{\text{OL}}}{\sigma_{\text{ys}}}\right)^2 \tag{3d}$$

where $\left(K_{\max}\right)_{\text{eff}}$ is the effective maximum stress intensity factor; $\left(K_{\max}\right)_{\text{th}}$ is the threshold stress intensity factor corresponding to the maximum stress intensity factor; $\left(K_{\max}\right)_{\text{OL}}$ is the maximum stress intensity factor of overload stress cycle; $Z_{\text{OL}}$ is the size of overload retardation zone; $\Delta a'$ is the incremental growth following the overload; $r_{\text{so}}$ is the overload shut-off ratio, which means crack stops growing when the overload reaches this certain value [17]; $\sigma_{\text{ys}}$ is the material's yield strength.

It is well known that there are geometric changes and permanent dented plastic zone on aluminium-alloy thin-sheets subjected to LVI loading. Compared to undamaged thin-sheets, geometric changes cause stress concentration of post-impact thin-sheets under external load, which accelerates the crack growth [14]. The previous test results also show that the retardation effect on FCG rate is triggered when the crack just enters dented plastic zone, and it disappears after the crack passes through dented plastic zone [8,14]. Moreover, the crack growth rate often reaches the minimum value at the centre site of the dent during the crack growth process in dented plastic zone. Therefore, characterising the FCG behaviours of aluminium-alloy thin-sheets with LVI damage needs to consider the effects of geometric changes and the dented plastic zone caused by LVI loading.

In terms of this, a Wheeler's retardation function $f(a)$ [18] with simple quadratic form from the dented plastic zone and an acceleration function $g(k_{tyy})$ with power function form from the stress concentration due to impact-induced geometric changes are introduced into the Eq. (2). Then the empirical FCG model considering the effects of load interaction and LVI damage is determined as

$$\frac{da}{dN}=\begin{cases} f(a)\,g(k_{tyy})C(\Delta K-\Delta K_{th})^{m_1}(1-R_{eff})^{m_2}, & \Delta K \geq \Delta K_{th} \\ 0, & \Delta K < \Delta K_{th} \end{cases} \tag{4}$$

with

$$f(a)=\begin{cases} \dfrac{1-m_0}{r_p^2}(a-a_{dent})^2+m_0, & \text{inner dented region} \\ 1, & \text{outer dented region} \end{cases} \tag{5}$$

$$g(k_{tyy})=\left[k_{tyy}(a)\right]^{m_1}=\left[\frac{\sigma_{yy}(a)}{\sigma_{nom}(a)}\right]^{m_1} \tag{6}$$

where $a$ is the crack size; $a_{dent}$ is the crack size at the centre site of impact dent; $r_p$ is the radius of dented plastic zone on post-impact aluminium-alloy thin-sheets, which can be assessed by experiment or finite element method; $m_0$ is the retardation coefficient of dented plastic zone, which is determined by constant amplitude FCG test results of the specimens with LVI damage. $k_{tyy}$ is the impact-induced stress concentration factor in the y-direction; $\sigma_{yy}(a)$ and $\sigma_{nom}(a)$ are the y-direction stresses in the potential crack growth path for the post-impact specimens and undamaged specimens, respectively, which can be determined by the finite element method; $m_1$ is the material constant in FCG model, which is determined from the constant amplitude FCG test data.

Taking transformation and integrating Eq. (4), we can get FCG increment for *i*-th stress cycle under random spectrum loadings, that is as follow:

$$\Delta a_i = \begin{cases} f\left(a_{i-1}\right) g\left(k_{\mathrm{tyy}}\left(a_{i-1}\right)\right) C\left(\Delta K_i - \Delta K_{\mathrm{th}}\right)^{m_1} \left(1 - R_{\mathrm{eff},i}\right)^{m_2} & , \Delta K_i \geq \Delta K_{\mathrm{th}} \\ 0 & , \Delta K_i < \Delta K_{\mathrm{th}} \end{cases} \tag{7}$$

According to Eq. (7), the FCG accumulative methodology is established to predict FCG life of post-impact aeronautic aluminium-alloy thin-sheets under spectrum loading, and the steps are as follow:

**(i)** Given the initial crack size $a_0$ and set $a = a_0$, the dent retardation function $f\left(a_0\right)$ and acceleration function $g\left(k_{\mathrm{tyy}}\left(a_0\right)\right)$ are determine by Eq. (5) and Eq. (6); then $R_{\mathrm{eff},1}$ corresponding to the first fatigue stress cycle in the loading spectrum are calculated by Eq. (3). Substituting $f\left(a_0\right)$, $g\left(k_{\mathrm{tyy}}\left(a_0\right)\right)$ and $R_{\mathrm{eff},1}$ into Eq. (7), crack growth increment $\Delta a_1$ corresponding to the first fatigue stress cycle can be determined, and then current crack size $a$ is updated by $a = a_0 + \Delta a_1$;

**(ii)** Similarly, according to Eq. (3), Eq. (5) and Eq. (6), $f\left(a_1\right)$, $g\left(k_{\mathrm{tyy}}\left(a_1\right)\right)$ and $R_{\mathrm{eff},2}$ corresponding to the second fatigue stress cycle in the loading spectrum can be determined. Substituting $f\left(a_1\right)$, $g\left(k_{\mathrm{tyy}}\left(a_1\right)\right)$ and $R_{\mathrm{eff},2}$ into Eq. (7), crack growth increment $\Delta a_2$ corresponding to the second fatigue stress cycle can be calculated, and then current crack size $a$ is updated by $a = a_1 + \Delta a_2$;

**(iii)** With such a cycle-by-cycle accumulation calculation, new crack growth increment on each subsequent adjacent fatigue stress cycle in the loading spectrum can be determined until final fracture and the cumulative number of fatigue stress cycle corresponding to each current crack size can be obtained and recorded. Obviously, the effects of load interaction and LVI damage are taken into account in the above crack growth accumulation calculations according to Eq. (7).

**(iv)** Finally, if fracture criterion ($a \geq a_{\mathrm{C}}$) is triggered in current crack size, the FCG failure of aluminium-alloy thin-sheets with LVI damage occurs and the predicted FCG life ($N_{\mathrm{f}}$) is the total accumulative fatigue cycles.

## 3. Experiments

### 3.1 Material and specimen

The test specimens are made of 7075-T62 aluminium-alloy, and the mechanical properties of 7075-T62 are presented in Table 1. Fig. 1(a) shows the geometric configuration and dimensions of the specimen. In order to obtain post-impact specimens, the LVI tests of pristine aluminium-alloy thin-sheet specimens were carried out on a drop-weight impact tester at room temperature and moisture (see Fig. 2), and the drop-weight has a mass of 8.25 kg or 8.29 kg with a hemispherical steel nose.

According to ASTM D7136 [19], the steel window frame with a 23.0 mm or 26.5 mm diameter central hole was firstly placed on the rigid base. The rubber plate with the white borderlines, used to locate the specimen in the correct position, was then fixed on the rigid base to avoid causing any scratches on the specimen. Subsequently, the centre position of the rigid base was adjusted to align the impact site. Next, the specimen was fully clamped within the white borderlines of the rubber plate on the rigid base using four steel bolts and the support fixture. During tests, all specimens were impacted by the free drop-weight at some specific impact energies, which were controlled by adjusting the height of the drop-weight. To simulate the common impact dent damage of aluminium-alloy aircraft skin in service, twelve impact energies were selected to obtain twelve kinds of post-impact specimens for two types of 7075-T62 aluminium-alloy thin-sheets (see Table 2). The notation of the specimen is explained by examples as follows: the specimen T1.6-D23-Q4.78J-1 means that the 1/4 point of the crack axis of the first specimen with the thickness of 1.6 mm is located on the rigid base with a 23 mm diameter central hole, and the specimen is impacted with the energy level of 4.78 J. The specimen T2.0-D23-C8.90J-2 indicates that the centre of the crack axis of the second specimen with the thickness of 2.0 mm is located on the rigid base with a 23 mm diameter central hole, and the specimen is impacted with the energy level of 8.90 J. Other specimen codes have similar meaning. Each group contained at least three specimens to ensure the reliability of the test data. Finally, the post-impact specimen was removed from the tester and the digital depth micrometre was employed to measure the indentation depth, which was the distance from the lowest point in the dent region to the horizontal plane of the specimen. Afterwards, a prefabricated crack starter notch with length of 20 mm and width of 0.5 mm was processed on the right edge of each specimen by electric-discharge machining for following FCG tests (see Figs. 1(b)-1(d)).

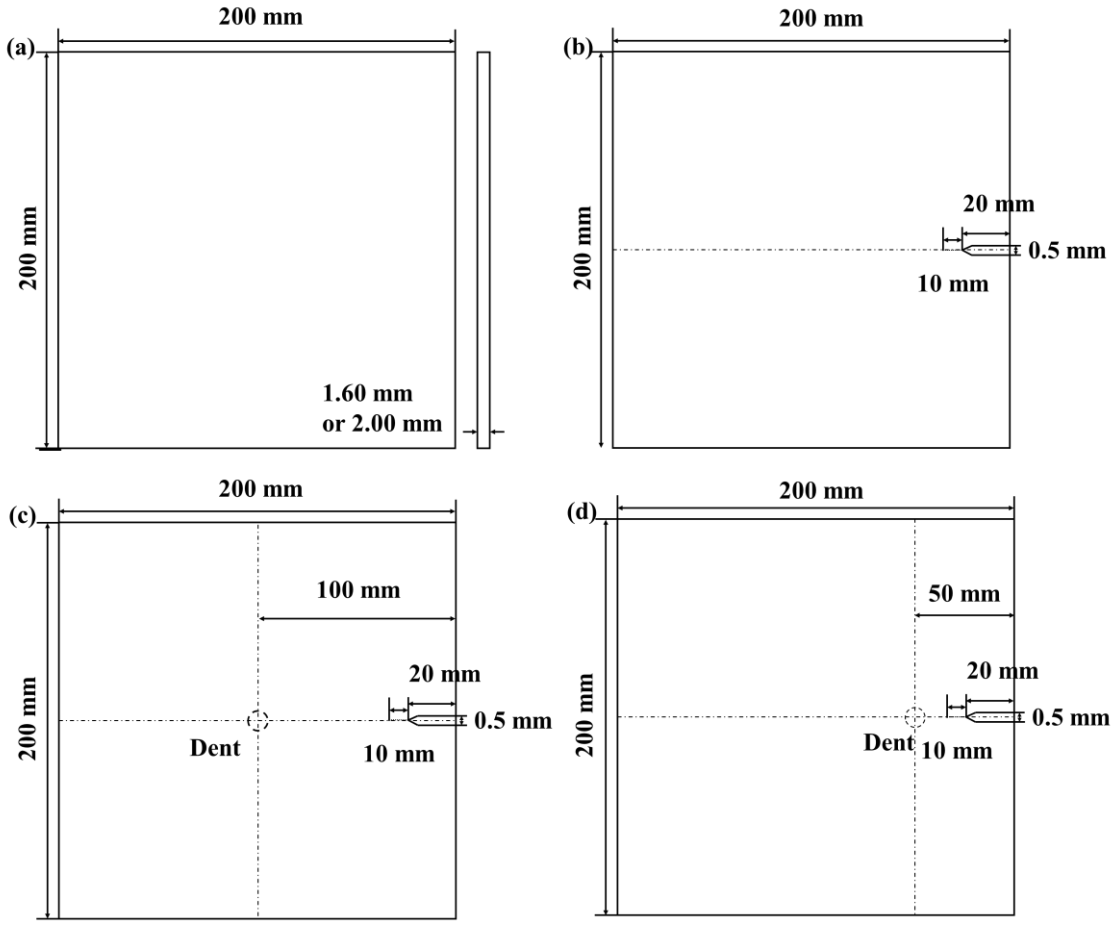


**Fig. 1** Geometric configuration and dimensions of specimens: (a) 7075-T62 specimen, (b) FCG specimen, (c) centre impacted FCG specimen, (d) off-centre (1/4 width to the centre) impacted FCG specimen.

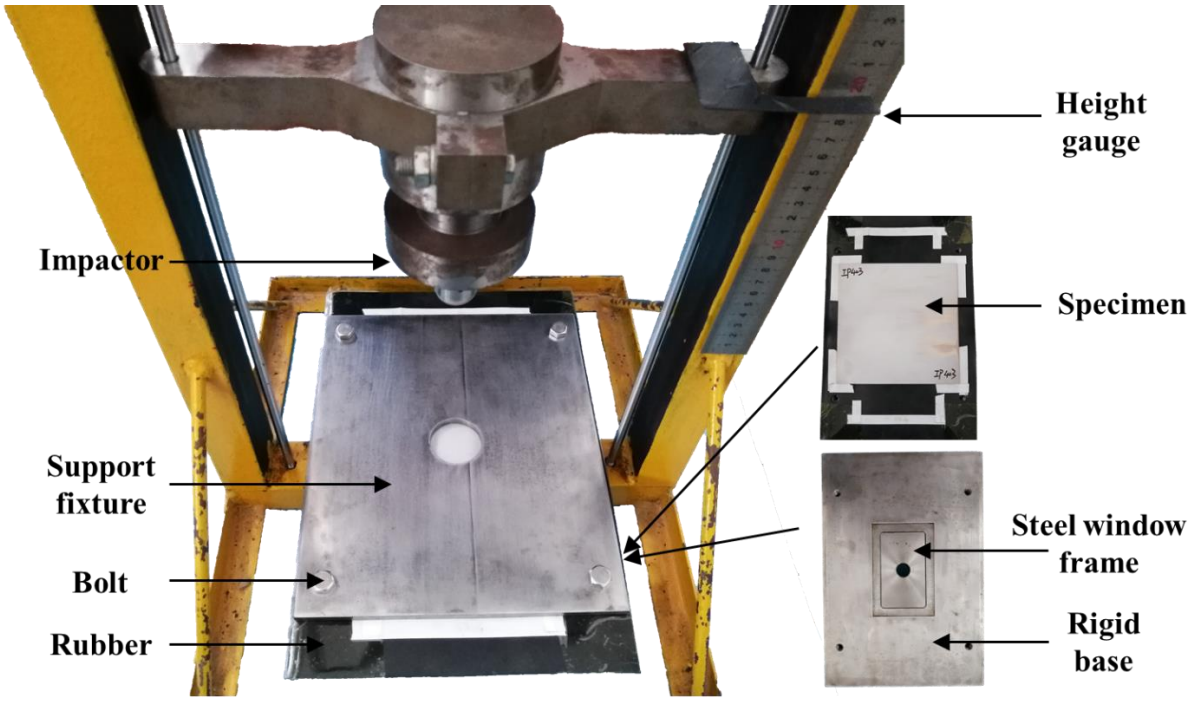


**Fig. 2** Drop-weight impact tester.

**Table 1** Mechanical properties of 7075-T62 [2,20]

| $E$ (MPa) | $\nu$ | $\rho$ (kg/m$^3$) | $\sigma_{ys}$ (MPa) | $K_C$ ( MPa$\sqrt{\text{m}}$ ) | Johnson-Cook material model | | | |
|---|---|---|---|---|---|---|---|---|
| | | | | | $A_1$ (MPa) | $B_1$ (MPa) | $C_1$ | $n_1$ |
| 71000 | 0.33 | 2800 | 504 | 88.64 ($\pm$6.89) | 546 | 678 | 0.0084 | 0.71 |

**Table 2** Test matrix of LVI

| Thickness T (mm) | Base hole diameter D (mm) | Impactor mass (kg) | Impact site (C or Q) | Impact energy (J) |
|---|---|---|---|---|
| 1.6 | 23 | 8.25 | centre (C) | 2.83,3.24,4.05,5.67 6.47,8.09,11.33,14.57 |
| | | | 1/4 width to the centre (Q) | 4.78 |
| | 26.5 | 8.29 | centre (C) | 17.08,19.52 |
| 2.0 | 23 | 8.25 | centre (C) | 8.90 |

### 3.2 FCG tests

According to ASTM E647 [21], all constant amplitude and block spectrum loading FCG tests were carried out on the QBS-100 KN servo-hydraulic tester under the sinusoidal waveform with a frequency of 10 Hz at room temperature and moisture (see Fig. 3). The upper and lower sides of the specimen were strengthened with aluminium-alloy sheets to reduce stress concentration at the clamped ends. During tests, the WZHD0850 long focal-length optical telemicroscope with 0.001 mm measurement resolution was utilised to measure the crack size at a specific interval of cyclic loading. A pre-crack of about 10 mm length on all specimens (see Figs. 1(b)-1(d)) was made to simulate the engineering crack with a sharp tip using multi-step decreasing fatigue loading. The experimental data $(a_i, N_i)$ were recorded and the FCG rate $(da/dN)_i$ corresponding to crack size $a_i$ can be determined by using the secant method. The finite element method was used to calculate the stress intensity factor of the non-standard specimen [22], and the stress intensity factor range was as follow:

$$\Delta K = Y \Delta\sigma \sqrt{\pi a} \tag{8}$$

with

$$Y = 0.99 - 7.10\left(\frac{a}{w}\right) + 45.12\left(\frac{a}{w}\right)^2 - 92.81\left(\frac{a}{w}\right)^3 + 81.85\left(\frac{a}{w}\right)^4 \tag{9}$$

where $w$ is the width of specimen.

There are three types of FCG tests, including **(i)** constant amplitude FCG tests for undamaged

aluminium-alloy thin-sheet specimens with the thickness of 1.6 mm and 2.0 mm under maximum fatigue stress of 55 MPa with the stress ratio of 0.1; **(ii)** constant amplitude FCG tests for post-impact specimens under maximum fatigue stress of 55 MPa with the stress ratios of 0.06, 0.1, 0.3, 0.5 and 0.7; **(iii)** four types of block spectra FCG tests for post-impact specimens. At least three specimens were employed for each FCG test to ensure the reliability of the test data.

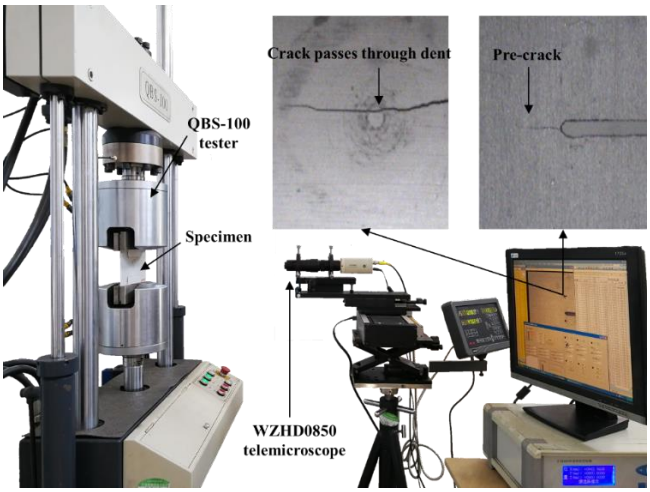


**Fig. 3** Fatigue crack growth test setups.

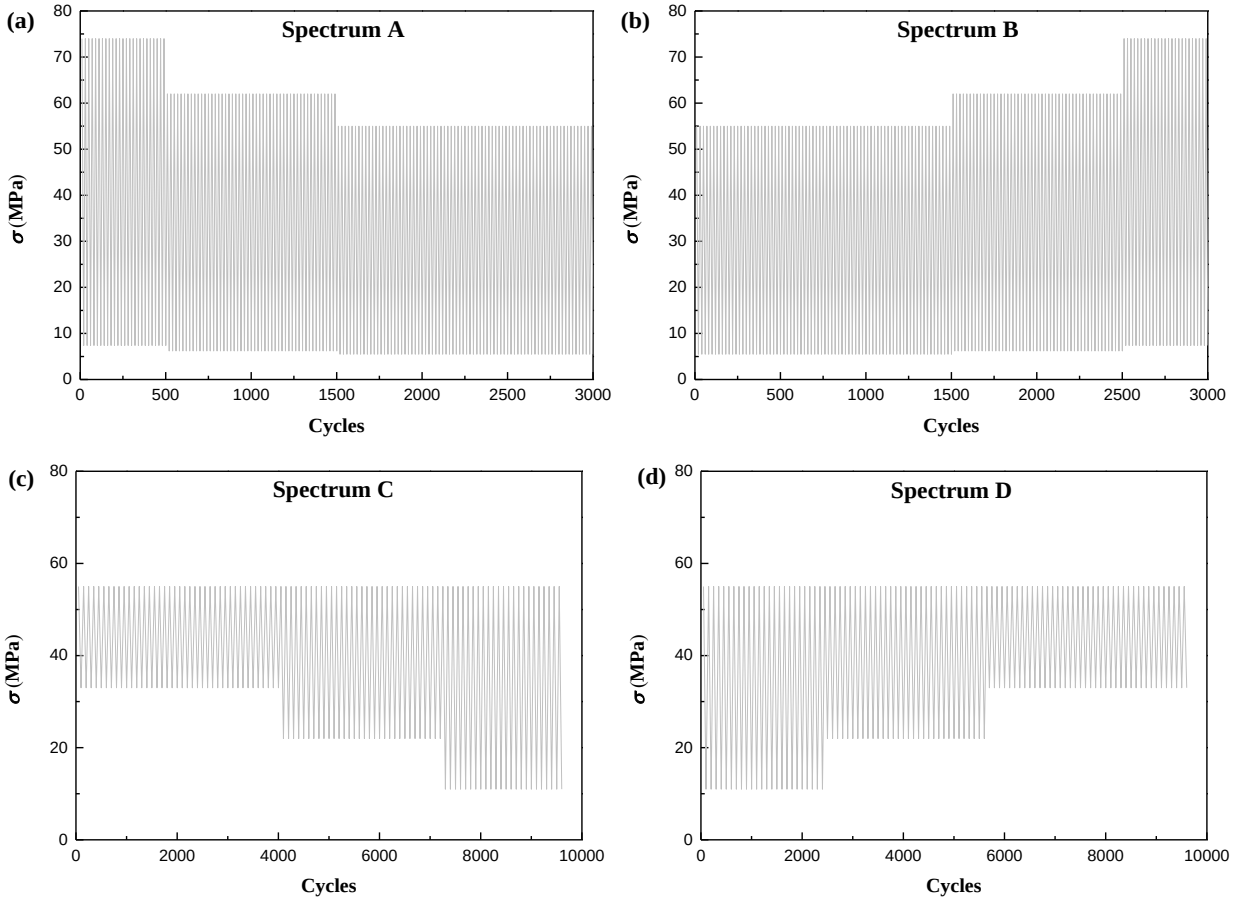


**Fig. 4** Block spectrum loading history for FCG specimens with LVI damage: (a) Spectrum A for T1.6-D23-C11.33J specimens, (b) Spectrum B for T1.6-D23-C6.47J specimens, (c) Spectrum C for

T2.0-D23-C8.90J specimens, (d) Spectrum D for T1.6-D26.5-C17.08J specimens.

### 3.3 Macroscopic failure analysis

The sketch diagram of the FCG topologies of 7075-T62 aluminium-alloy thin-sheet specimens is shown in Fig. 5. The typical FCG topologies of the specimens under constant amplitude and block spectrum loading are shown in Figs. 6 and 7, respectively. Tables 3 and 4 list the FCG live of the specimens under constant amplitude and block spectrum loading. From Figs. 5-7, as well as Tables 3 and 4, four major findings are as follows:

**(1)** Different from undamaged aluminium-alloy thin-sheet specimens (see Fig. 5(a)), the macroscopic FCG topologies of the specimens with LVI damage contains three types: crack through dent centre or called Type I crack (see Fig. 5(b)), crack across dent edge or named Type II crack (see Fig. 5(c)) and crack bypassing the dent or termed Type III crack (see Fig. 5(d)). The crack usually grows in Type I mode on the aluminium-alloy thin-sheet specimens due to the larger dented plastic zone caused by LVI with the higher impact energy level (see Figs. 6(b)-6(h)), while the crack always grows in Type II and Type III modes on the specimens due to the smaller dented plastic zone induced by LVI with lower impact energy levels (see Figs. 6(i)-6(l)) .

**(2)** Under the constant amplitude fatigue load with maximum fatigue stress of 55 MPa and stress ratio of 0.1, the FCG life of undamaged specimens (see Fig. 6(a)) is 61026 cycles (see Table 3). When cracks went through the dent centre of 4.78 J, 8.09 J and 14.57 J impacted specimens during the crack growth process (see Figs. 6(b)-6(d)), cracks grow in the Type I-dominated mode. The FCG life of these specimens are 75428, 85572, 77478 cycles (see Table 3), respectively, which is longer than the life of undamaged specimens. It indicates that LVI damage can extend the FCG life of aluminium-alloy thin-sheet specimens in case of the crack growth in the Type I-dominated mode. This is because dented plastic zone has a significant retardation effect on crack growth rate.

**(3)** Under the constant amplitude fatigue load with maximum fatigue stress of 55 MPa and stress ratio of 0.1, the fatigue cracks of the 3.24J impacted specimens ran through the dent edge (Type II, see Fig. 6(i)) or bypassed the dent (Type III, see Fig. 6(k)). The FCG life of the specimens is 56069 cycles (see Table 3), which is shorter than the life of undamaged specimens. Moreover, under the constant amplitude fatigue load with maximum fatigue stress of 55 MPa and stress ratio of 0.5, the cracks of two 4.05J impacted specimens also passed dent edge (see Fig. 6(j)) or bypassed the dent (see Fig. 6(l)). The FCG life of these two specimens are lower than that of specimens on which the crack grows in Type I mode (see Fig. 6(g) and Table 3). It demonstrates that the LVI damage can shorten the FCG life of aluminium-alloy thin-sheet specimens in case of the crack growth in Type II and Type III modes. The reason is that the geometric changes induced by LVI lead to stress

concentration which has a considerable acceleration effect on the crack growth rate.

**(4)** Under the block spectrum fatigue load, there are two types of macroscopic FCG topologies of the post-impact aluminium-alloy thin-sheet specimens due to the limited specimen numbers, including crack through dent centre (Type I crack, see Figs. 7(a)-7(c)) and crack across dent edge (Type II crack, see Figs. 7(d)-7(i)). The crack grew in Type I-dominated mode on the post-impact specimens under Spectrum A and Spectrum D loading due to the larger dented plastic zone of the specimens. Under Spectrum B and Spectrum C loading, due to the smaller dented plastic zone of the specimens, the crack grew in Type II-dominated mode on the post-impact specimens. The FCG life of post-impact specimens with Type I crack is more than that with Type II crack under Spectrum B loading (see Table 4), which is similar to the constant amplitude FCG results.

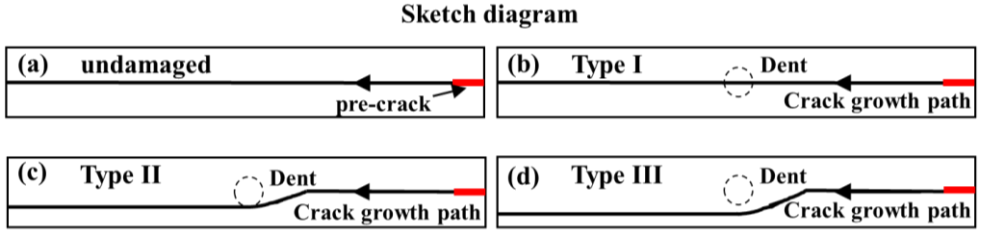


**Fig. 5** Sketch diagram of FCG topologies.

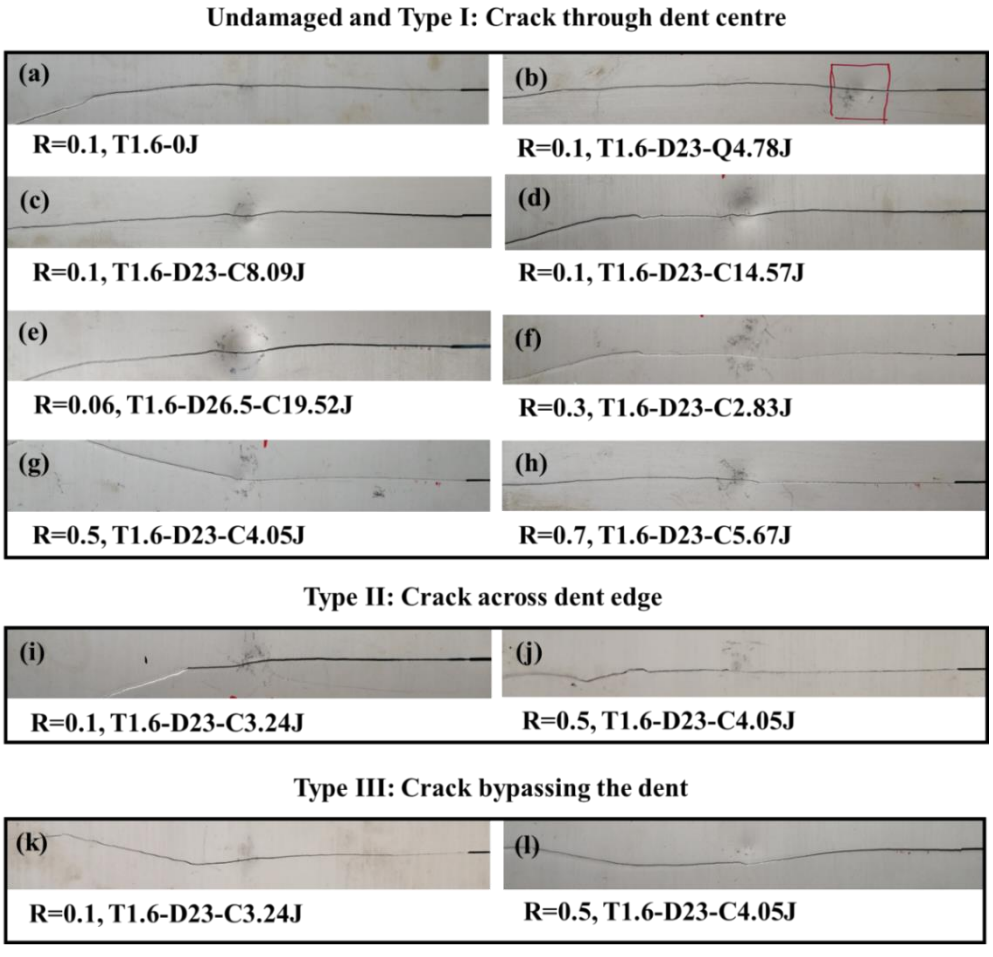


**Fig. 6** Typical macroscopic FCG topologies under constant amplitude FCG tests.

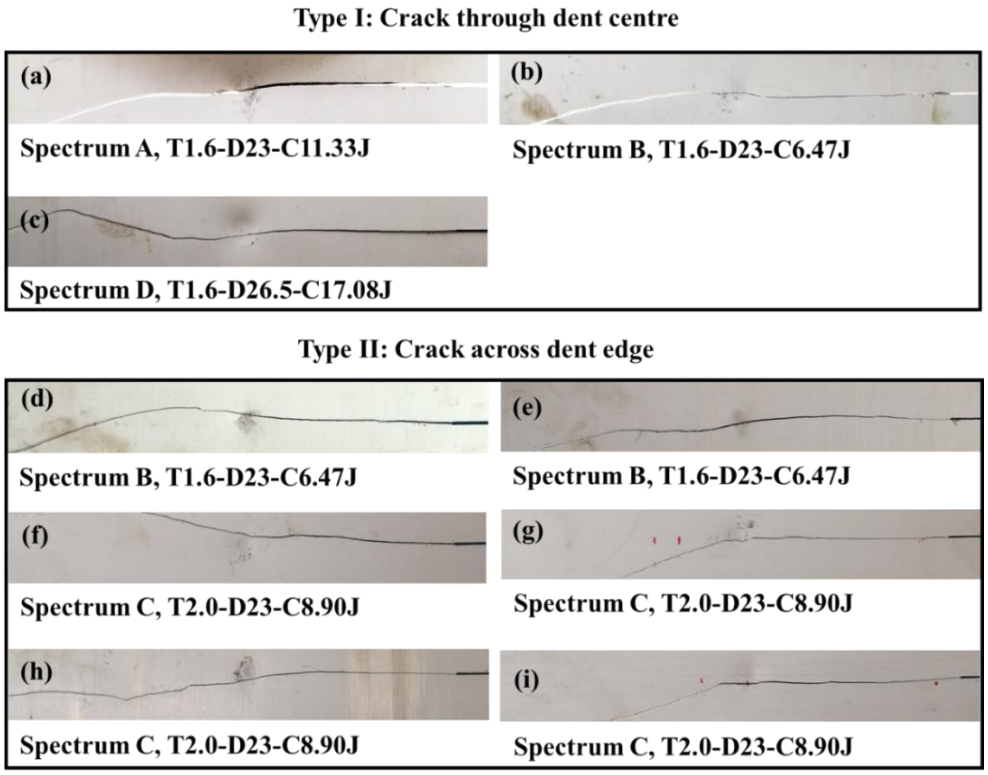


**Fig. 7** Typical macroscopic FCG topologies under block spectrum loading FCG tests.

**Table 3** Comparison between experimental and prediction constant amplitude FCG life (Maximum fatigue stress 55 MPa)

| Crack topologies | Stress Ratio | Specimen type | Average $a_0$ (mm) | $r_p$ (mm) | Tests (cycles) | Mean Value (cycles) | Predictions (cycles) | Relative Deviation |
|---|---|---|---|---|---|---|---|---|
| Type I: Crack through dent centre | 0.1 | T1.6-0J and T2.0-0J | 30.31 | 0 | 70717<br>68671<br>58723<br>45993 | 61026 | 68745 | 12.7% |
| | | T1.6-D23-Q4.78J | 31.26 | 12.50 | 75734<br>71328<br>79221 | 75428 | 63659 | 15.6% |
| | | T1.6-D23-C8.09J | 31.16 | 16.45 | 81938<br>92182<br>82595 | 85572 | 84905 | 0.8% |
| | | T1.6-D23-C14.57J | 31.46 | 19.61 | 85425<br>65973<br>81037 | 77478 | 75937 | 2.0% |
| | 0.06 | T1.6-D26.5-C19.52J | 30.42 | 22.83 | 69039<br>80093 | 74566 | 79564 | 6.7% |
| | 0.3 | T1.6-D23-C2.83J | 30.31 | 8.03 | 126383<br>99469<br>113318 | 113057 | 129090 | 14.2% |
| | 0.7 | T1.6-D23-C5.67J | 37.78 | 13.47 | 198608<br>175323 | 195855 | 188036 | 4.0% |

| | | | | | | | | |
|---|---|---|---|---|---|---|---|---|
| | | | | | 213633 | | | |
| Type II and Type III: Crack across dent edge or Crack bypassing the dent | 0.1 | T1.6-D23-C3.24J | 30.24 | 8.53 | $53480^{II}$<br>$58658^{III}$ | 56069 | 67889 | 21.1% |
| | 0.5 | T1.6-D23-C4.05J | 30.46 | 10.50 | $132783^{I}$<br>$126513^{II}$<br>$109220^{III}$ | 122839 | 143392 | 16.7% |
| Note: i) I means Type I mode; II means Type II mode; III means Type III mode.<br>ii) The retardation function $f(a)$=1 for the Type II and Type III modes. | | | | | | | | |

**Table 4** Comparison between experimental and prediction block spectrum loading FCG life

| Crack topologies | Load history | Specimen type | Average $a_0$ (mm) | $r_p$ (mm) | Tests (blocks) | Mean Value (blocks) | Predictions (blocks) | Relative Deviation |
|---|---|---|---|---|---|---|---|---|
| Type I: Crack through dent centre | Spectrum A | T1.6-D23-C11.33J | 29.96 | 18.53 | 20.27<br>20.00<br>10.79<br>11.21 | 15.57 | 17.12 | 10.0% |
| | Spectrum D | T1.6-D26.5-C17.08J | 30.45 | 21.73 | 13.57<br>10.04<br>20.38 | 14.66 | 15.54 | 6.0% |
| Type II: Crack across dent edge | Spectrum B | T1.6-D23-C6.47J | 30.03 | 14.44 | $17.75^{I}$<br>16.88<br>16.08 | 16.90 | 18.46 | 9.2% |
| | Spectrum C | T2.0-D23-C8.90J | 30.87 | 14.43 | 12.74<br>12.15<br>11.42<br>10.25 | 11.64 | 12.46 | 7.1% |
| Note: i) I means Type I mode; ii) The retardation function $f(a)$=1 for the Type II modes. | | | | | | | | |

### 3.4 Experimental results and analysis

Fig. 8 presents the constant amplitude FCG $a$-$N$ experimental data of the 7075-T62 aluminium-alloy thin-sheets. From the $a$-$N$ data shown in Fig.8, the $da/dN$-$\Delta K$ data can be determined by Eq. (12), and are shown in Fig. 9. From Figs. 8 and 9, five main findings can be obtained as follows:

**(1)** There is a little difference in the $a$-$N$ data for the undamaged aluminium-alloy thin-sheet specimens with thickness of 1.6 mm and 2.0 mm (see Fig. 8(a)). The main reasons of this are as follow: **i)** pre-crack length directly affects the current crack growth rate and final fatigue life; however, it is difficult to make the pre-crack length being same under manual operation even for the undamaged specimens; **ii)** specimens' performance differences due to manufacturing would affect the crack propagation. The cracks in different specimens, e.g., four undamaged specimens, sometimes deflect their growth direction to varying extents, but the nominal crack length in record is the horizontal distance from the origin, this also contributes to the data scatter. In spite of this, the $da/dN$-$\Delta K$

curves for two types of specimens are almost identical (see Fig. 9(a)), which illustrates that there is no significant difference for the FCG properties between 1.6mm and 2.0 mm thickness 7075-T62 aluminium-alloy thin-sheets.

**(2)** Stress ratio has a significant effect on the FCG rate of aluminium-alloy thin-sheets. There is no major difference for the FCG data at the stress ratios between 0.06 and 0.1, while the $da/dN$-$\Delta K$ data gradually moves to the upper left as the stress ratio increases from 0.1 to 0.7 (see Fig. 9(b)). Therefore, it is necessary to account for the stress ratio effect in characterising the FCG behaviours of aluminium-alloy thin-sheets.

**(3)** When the crack grows in Type I mode on the post-impact specimens at dented plastic zone, the slope of $a$-$N$ data for these specimens first decreases gradually (see Figs. 8(c) and 8(d)), and reaches minimum values at about the dent centre (50 mm for off-centre impacted specimens and 100 mm for centre impacted specimens), after that, the slope gradually increases. There are no significant changes in the slope of $a$-$N$ data within dented plastic zone range for the specimens on which the crack grows in Type II and Type III modes because the crack grows outside dented plastic zone (see Fig. 8(b)). More $a$-$N$ data are given in Appendix B.

**(4)** There are three crack growth stages for the centre impacted specimens with Type I crack (see Fig.9 (c)). **i)** At stage I far from dented plastic zone, the $da/dN$-$\Delta K$ data for undamaged and post-impact aluminium-alloy thin-sheets basically coincide, which shows that the LVI damage has no significant effect on the crack growth rate within this stage. **ii)** At stage II close to dented plastic zone, the slope of $da/dN$-$\Delta K$ data of post-impact specimens is greater than that of undamaged specimens. The reason is that the geometry of post-impact specimens has changed compared to undamaged specimens, which leads to serious stress concentration, so the FCG rate becomes greater at this stage. Therefore, it is necessary to consider the stress concentration effect due to the geometric changes induced by LVI into the FCG model for post-impact aluminium-alloy thin-sheets. **iii)** At stage III in dented plastic zone, dented plastic zone has a significant retardation effect on the crack growth rate. Specifically, the crack growth rate within this region firstly gradually decreases and reaches minimum value at dent centre, then gradually increases. The general trend of crack growth rate at this stage is a parabolic shape, which justifies the dent retardation function in Section 2.

**(5)** There are four crack growth stages for off-centre impacted specimens with Type I crack (see Fig.9 (d)). **i)** At stage I, the LVI damage has no significant effect on the crack growth rate. **ii)** At stage II, the slope of $da/dN$-$\Delta K$ data of post-impact specimens is greater than that of undamaged specimens due to the stress concentration introduced by impact-induced geometric changes. **iii)** At stage III,

crack growth rate first decreases and then gradually increases due to the retardation effect of dented plastic zone. **iv)** At stage IV after passing through dented plastic zone, crack growth rate restores to the level of undamaged specimens due to the loss of retardation effect of dented plastic zone.

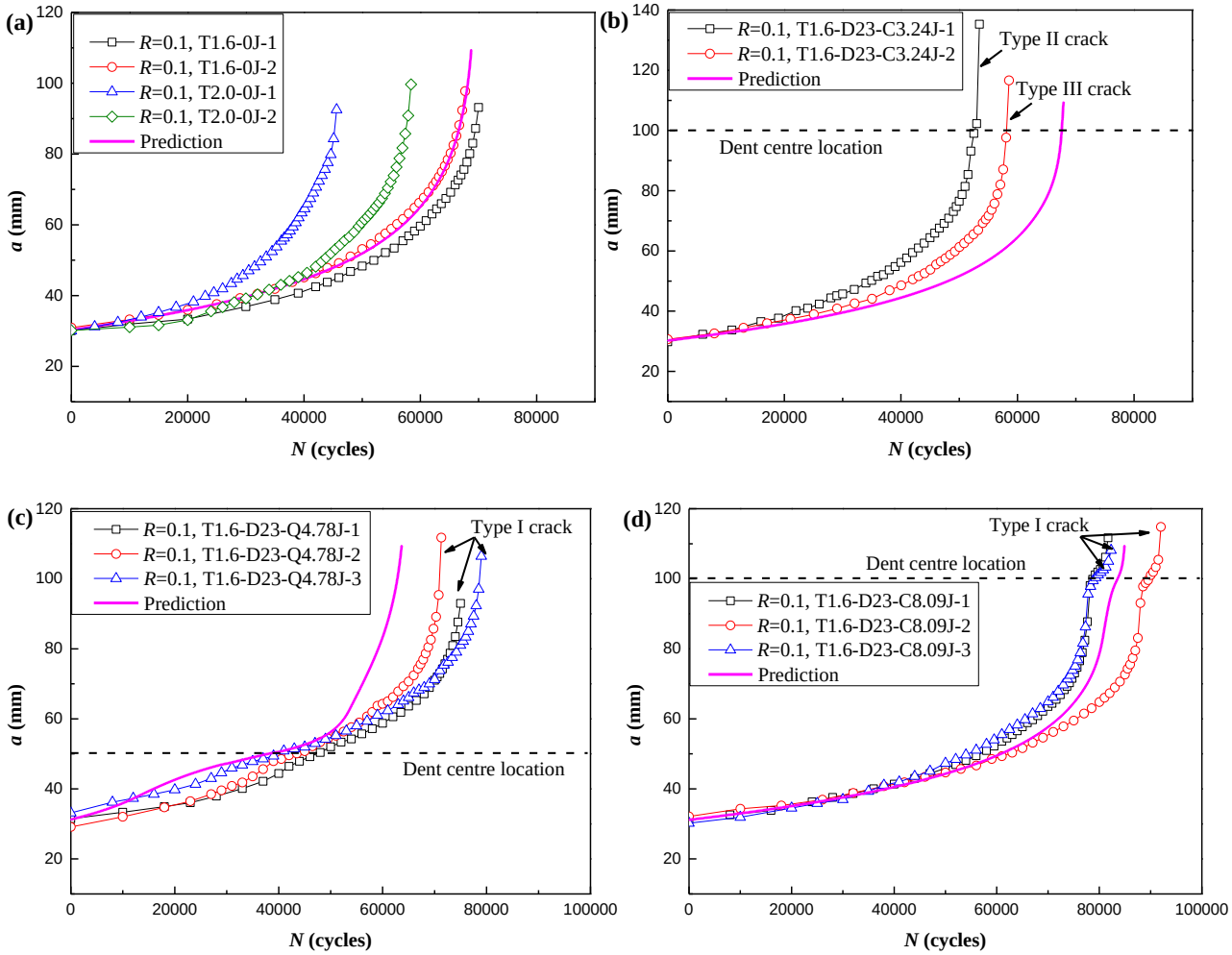


**Fig. 8** Comparison between predicted and experimental constant amplitude FCG *a*-*N* data at *R*=0.1: (a) T1.6-0J and T2.0-0J specimens; (b) T1.6-D23-C3.24J specimens; (c) T1.6-D23-Q4.78J specimens; (d) T1.6-D23-C8.09J specimens.

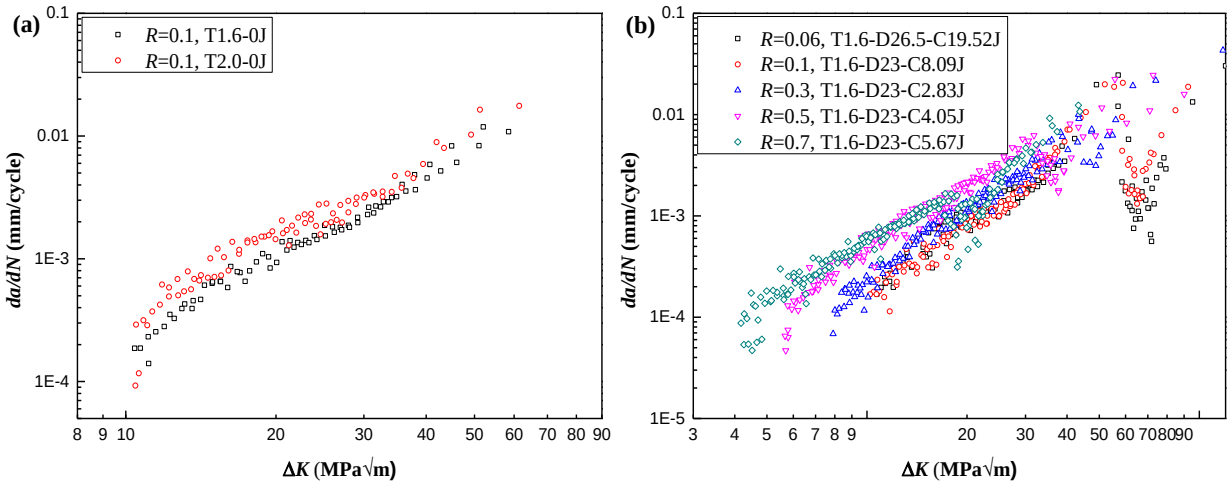

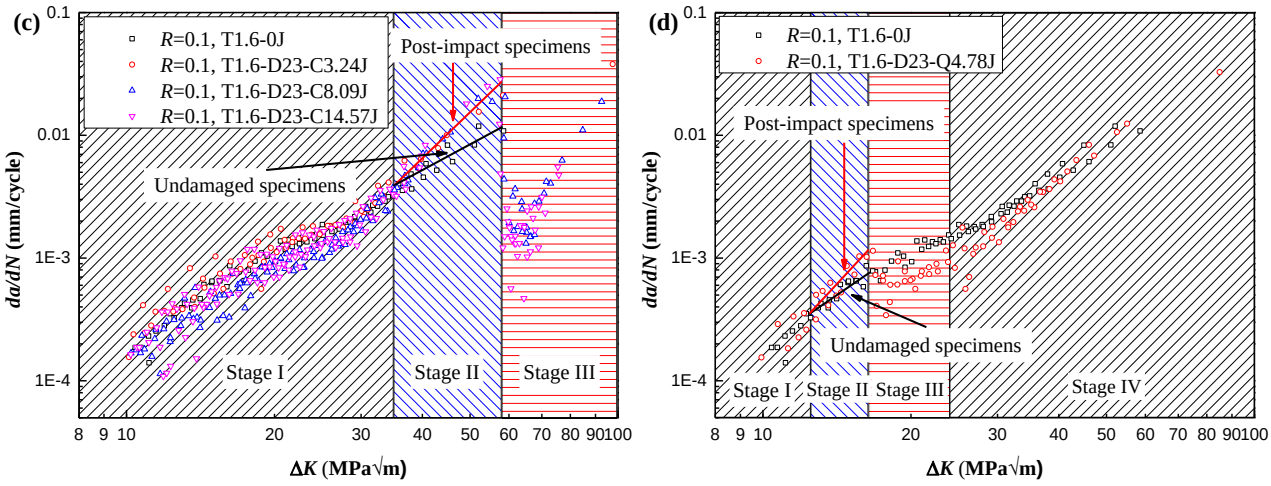


**Fig. 9** Nominal constant amplitude FCG $da/dN$-$\Delta K$ data: (a) different specimen thickness at $R$=0.1; (b) different stress ratios; (c) different impact energies at $R$=0.1; (d) off-centre impacted specimens at $R$=0.1.

## 4. Model verification

### 4.1 Calculation of dented plastic zone and stress concentration factor

In order to predict the FCG life of post-impact aluminium-alloy thin-sheets, the formulations of the FCG model considering the effects of load interaction and LVI damage are proposed in Section 2. Two key parameters used in the model are the size of dented plastic zone and stress concentration factor introduced by geometric changes, which are difficult to measure from experiments accurately and are dependent on the boundary conditions. This part aims to determine the size of dented plastic zone and stress concentration factor numerically by finite element analysis. The finite element method (FEM) also facilitates a fully predictive framework to predict the FCG life without the need of further experiments.

The 3D element C3D8R are employed to model aluminium-alloy thin-sheet specimens, rigid base, support fixture, bolts and rubber plate, and the total element number is 96675. Moreover, rigid element R3D4 is used to model hemispherical impactor, and the number of elements is 1054. Thus, a 3D nonlinear elastic-plastic finite element model (shown in Fig. 10a) is generated by Abaqus/explicit code to estimate permanent plastic deformation, based on the Johnson-Cook constitutive model [23], which can be written as

$$\sigma_{\mathrm{fs}} = \left(A_1 + B_1 \cdot \varepsilon^{n_1}\right)\left(1 + C_1 \ln \frac{\dot{\varepsilon}}{\dot{\varepsilon}_0}\right) \tag{10}$$

where $\sigma_{\mathrm{fs}}$ is the flow stress; $\varepsilon$ is the equivalent plastic strain; $\dot{\varepsilon}$ is the reference ratio of plastic strain; $A_1$, $B_1$, $C_1$ and $n_1$ are material parameters of 7075-T62 aluminium-alloy thin-sheets (listed in Table 1). The material properties of other components are listed in Table 5. The boundary

conditions in the LVI model are defined as the clamped constraints on rigid base and bolts. The inertial mass and impact velocity are loaded at the tip of the impactor for modelling the specific impact energy. The face-to-face interaction method is adopted to define the interaction between the different components. Tangential "penalty contact" with a friction coefficient of 0.9 is used for the contact faces from rubber plate to specimen and rigid base, and the friction coefficient of 0.1 is used for other contact faces. Besides, the normal "hard contact" allowing separation after contact is used for all contact faces [24]. The computational details are listed in Table 6. It takes about 6110 seconds to run the LVI for impact duration of 7 ms.

The FEM of LVI has been validated in authors' previous work [2]. In addition, the scanning electron microscope analysis results demonstrate that the fatigue origins are located on the impact front surface of post-impact aluminium-alloy thin-sheet specimens. It is reasonable to suggest that the plastic zone located on the impact front surface of post-impact specimens has a dominant effect on the FCG behaviours. The equivalent plastic strain of post-impact specimen on Path 1 shown in Fig. 10(b) is exported due to the specimen's symmetry, and then the radius of dented plastic zone is determined based on material plasticity criterion, when equivalent plastic strain is greater than zero. Fig. 11 and Table 7 show the experimental and predicted results of indentation depth for different impact energies, as well as the calculated values of the radius of dented plastic zone. From Fig. 11 and Table 7, we can find that: **i)** The predicted dent depths are in good agreement with the test results for twelve types of post-impact specimens, and the maximum relative deviation between experiments and predictions is 12.1%, with an acceptable scatter, which illustrates the effectiveness and validity of the FEM again. **ii)** The calculated radius of dented plastic zone for post-impact specimens gradually increases and tends to reach a plateau with the increasing impact energy.

In order to calculate the stress concentration factor $k_{tyy}$, the post-impact specimen with deformed geometry obtained from the LVI simulation results is imported into the Abaqus/standard, and then the specimen model is assembled with four-reinforcement model to establish the static tension FEM (see Fig. 10(c)). The element C3D8R are employed to model aluminium-alloy thin-sheet specimen and reinforcements, and the total element number is 50414. A corresponding reference point is created and coupled with each reinforcement. The two lower reference points are clamped to model the boundary constraints, and static tensile loading of 55 MPa is applied on the two upper reference points in force. It just costs about 54 seconds (see Table 6) to calculate the stress concentration factor $k_{tyy}$ along the potential crack growth path (see Path 1 in Fig. 10(b)) for post-impact specimens, as shown in Fig. 12. From Fig. 12, we can get: **i)** When the impact energy is lower than 4.05 J, the stress concentration factor $k_{tyy}$ monotonically decreases with the increase of the distance away from the

dent centre. **ii)** When the impact energy is higher than 4.05 J, the stress concentration factor $k_{tyy}$ firstly increases and then decreases with the increasing distance away from the dent centre. Moreover, the peak $k_{tyy}$ value gradually increases and its position gradually moves away from the dent centre as the impact energy increases.

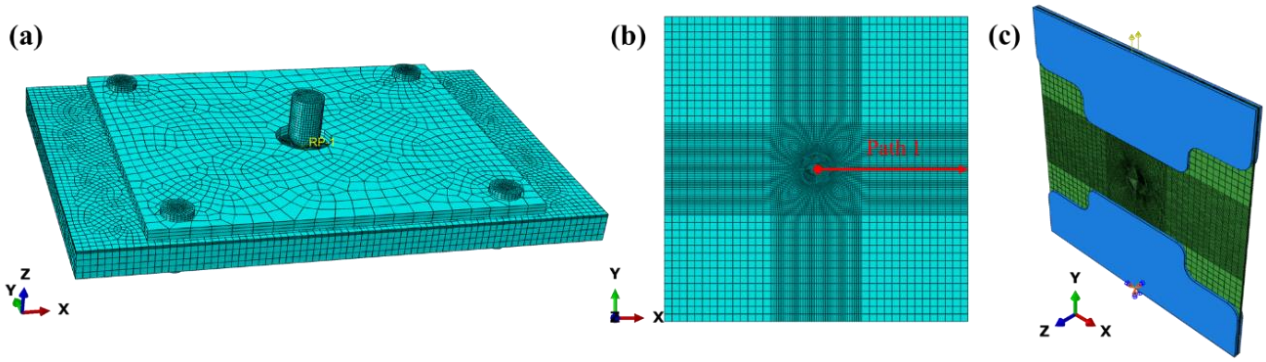


**Fig. 10** FE model:(a) LVI model, (b) specimen and path1, (c) static tension model.

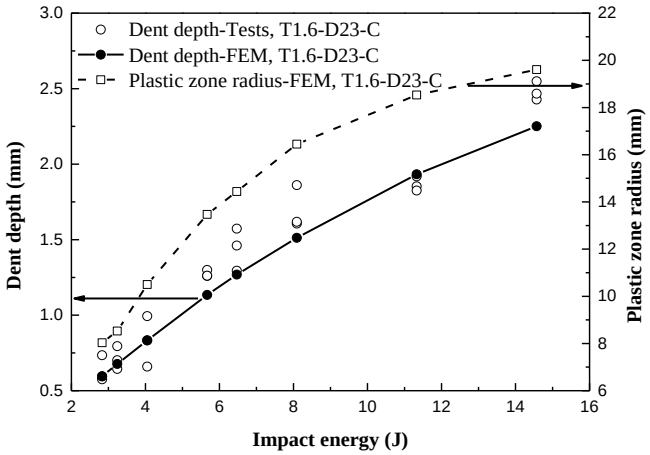


**Fig. 11** Dent depth and plastic zone radius.

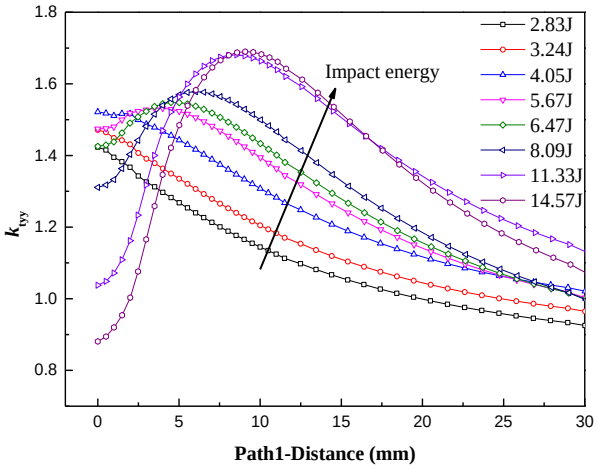


**Fig. 12** $k_{tyy}$ along path1 for T1.6-D23-C specimens.

**Table 5** Material properties used in LVI model

| Material | $\rho$ (kg/m$^3$) | Yeoh material model[25] | | |
|---|---|---|---|---|
| | | $C_{10}$ (MPa) | $C_{20}$ (MPa) | $C_{30}$ (MPa) |
| Rubber | 1100 | 0.55 | -0.05 | 0.95 |
| Material | $\rho$ (kg/m$^3$) | $E$ (MPa) | $\nu$ | |
| Bolt<br>Rigid base<br>Support fixture | 7850 | 210000 | 0.3 | |

**Table 6** Computational details for the LVI and SCF calcultions.

| Processor | RAM | CPU number | CPU time(s) | |
|---|---|---|---|---|
| | | | LVI calculation | SCF calculation |
| Intel Core i7-9750H 2.60GHz | 16 GB | 4 | 6110 | 54 |

**Table 7** Experimental and numerical results of LVI

| Specimen Type | Impact energy (J) | Dent depth experiments (mm) | Means (mm) | Predictions (mm) | Relative deviation | Plastic zone radius (mm) |
|---|---|---|---|---|---|---|
| T1.6-D23-C | 2.83 | 0.735,0.576,0.594 | 0.635 | 0.596 | 6.1% | 8.03 |
| | 3.24 | 0.795,0.702,0.644 | 0.714 | 0.677 | 5.2% | 8.53 |
| | 4.05 | 0.659,0.833,0.994 | 0.829 | 0.833 | 0.5% | 10.50 |
| | 5.67 | 1.299,1.260,1.262 | 1.274 | 1.134 | 11.0% | 13.47 |
| | 6.47 | 1.294,1.461,1.573 | 1.443 | 1.269 | 12.1% | 14.44 |
| | 8.09 | 1.607,1.618,1.861 | 1.695 | 1.512 | 10.8% | 16.45 |
| | 11.33 | 1.853,1.825,1.919,2.124 | 1.930 | 1.933 | 0.1% | 18.53 |
| | 14.57 | 2.428,2.549,2.467 | 2.481 | 2.251 | 9.3% | 19.61 |
| T1.6-D23-Q | 4.78 | 1.055,1.117,0.998 | 1.057 | 0.967 | 8.5% | 12.50 |
| T1.6-D26.5-C | 17.08 | 2.563,2.561,2.498 | 2.541 | 2.544 | 0.1% | 21.73 |
| | 19.52 | 2.939,2.817,2.816 | 2.857 | 2.758 | 3.5% | 22.83 |
| T2.0-D23-C | 8.90 | 1.267,1.116,1.219,1.390 | 1.248 | 1.199 | 3.9% | 14.43 |

### 4.2 Model characterisation and life prediction results

Based on constant amplitude FCG experimental data (see Fig. B2), the Least Squares Fitting method (see Appendix A) is used to obtain the FCG properties of 7075-T62 aluminium-alloy thin-sheets, that is

$$\frac{da}{dN}=1.77\times10^{-6}\left(\Delta K-0.73\right)^{2.13}\left(1-R\right)^{-0.97} \tag{11}$$

The $da/dN$-$\Delta K$-$R$ surface determined by Eq. (11) correlates well with test results (see Fig. 13), indicating that it is effective for $da/dN$-$\Delta K$-$R$ surface model in Eq. (1) to characterise FCG properties of 7075-T62 aluminium-alloy thin-sheets.

From the fracture toughness $K_{\mathrm{C}}$ of 7075-T6 aluminium-alloy sheets under plane stress conditions (see Table 1), the critical crack size $a_{\mathrm{c}}$ of post-impact specimens can be determined as follow:

$$a_{\mathrm{c}}=\frac{1}{\pi}\left(\frac{K_{\mathrm{C}}}{\sigma_{\max}Y\left(a_{\mathrm{c}}\right)}\right)^{2} \tag{12}$$

According to Eq. (9) and Eq. (12), the $a_{\mathrm{c}}$ value is calculated by the iterative algorithm (see Table 8). Then the retardation coefficient of dented plastic zone $m_0$ is determined by the ratio of the test

values of the FCG rate at dent centre (see Fig. 9(c)) and the acceleration function values times calculated values in Eq. (11) for post-impact T1.6-D23-C14.57 J specimens (see Table 8). Based on Eq. (5) to Eq. (7) and Eq. (11), we can obtain the FCG increment $\Delta a_i$ under a single fatigue stress cycle (see Table 9). The FCG model according to the FCG accumulative methodology can be used to predict the constant amplitude FCG *a-N* histories and life of post-impact 7075-T62 aluminium-alloy thin-sheet specimens (see Fig. 8, Fig. 14(a), Fig. B1 and Table 3). Moreover, the FCG model are adopted to predict the block spectrum FCG life of post-impact specimens (see Fig. 14 (b) and Table 4). Noticeably, the retardation function equals one for the Type II and Type III cracks because the crack deflects around the dent region, without retardation effect. From Figs. 8, 14 and B1, Tables 3 and 4, it is evident that:

**(1)** Under the constant amplitude fatigue load, calculated *a-N* histories for undamaged and post-impact aluminium-alloy thin-sheet specimens using the FCG model proposed in this paper correlate well with the experiments. The maximum relative deviations between FCG life predictions and experiments in case of undamaged specimens (see the test group S1 in Fig. 14(a)), post-impact specimens with Type I crack (see the test groups S2 to S7 in Fig. 14(a)), and post-impact specimens with Type II or Type III cracks (see the test groups S8 and S9 in Fig. 14(a)) are 12.7%, 15.6% and 21.1%, respectively, with acceptable accuracy. This indicates that the proposed FCG model are available to calculate crack growth histories and predict the FCG life of post-impact aluminium-alloy thin-sheets for all crack propagation types under the constant amplitude fatigue load. Noticeably, there is a certain difference between the predicted and experimental *a-N* histories for Type II and III cracks (see Fig. 8(b) and Fig. B1(d)), and the experimental FCG life is shorter than predictions (see Table 3). The main reason for this is likely that Type II and III cracks deflect around the dent region, causing the crack propagation path to deviate seriously from the predetermined trajectory. In this case, the stress concentration factor around the dent region is greater than that in the path through the dent centre, so the test FCG life is shorter than predictions.

**(2)** Under the block spectrum fatigue load, the maximum relative deviations between FCG life predictions and experiments in case of post-impact specimens with Type I crack (see Spectrum A and Spectrum D in Fig. 14(b)), and post-impact specimens with Type II (see Spectrum B and Spectrum C in Fig. 14(b)) are 10.0% and 9.2%, respectively, with an acceptable scatter. It demonstrates that the proposed FCG model considering the effects of load interaction and LVI damage in this paper is suitable for predicting crack growth life of aluminium-alloy thin-sheets with LVI damage for all crack propagation types under the block spectrum fatigue load.

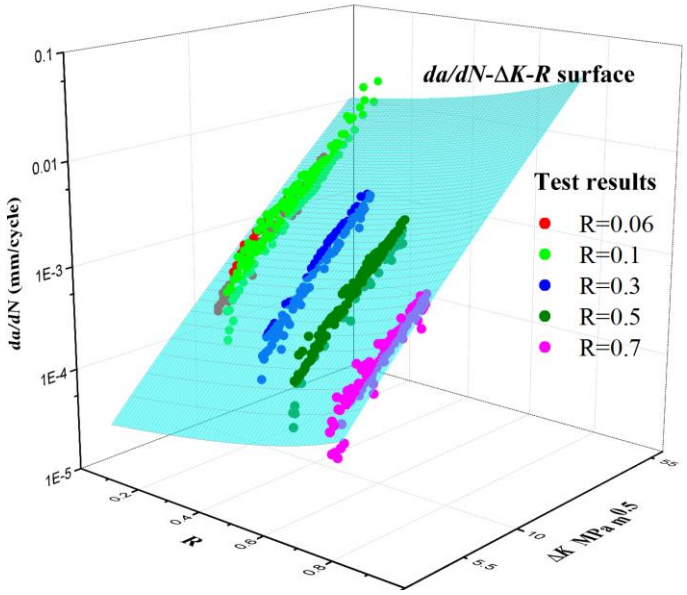


**Fig. 13** Crack growth rate $da/dN$ -$\Delta K$-$R$ surface.

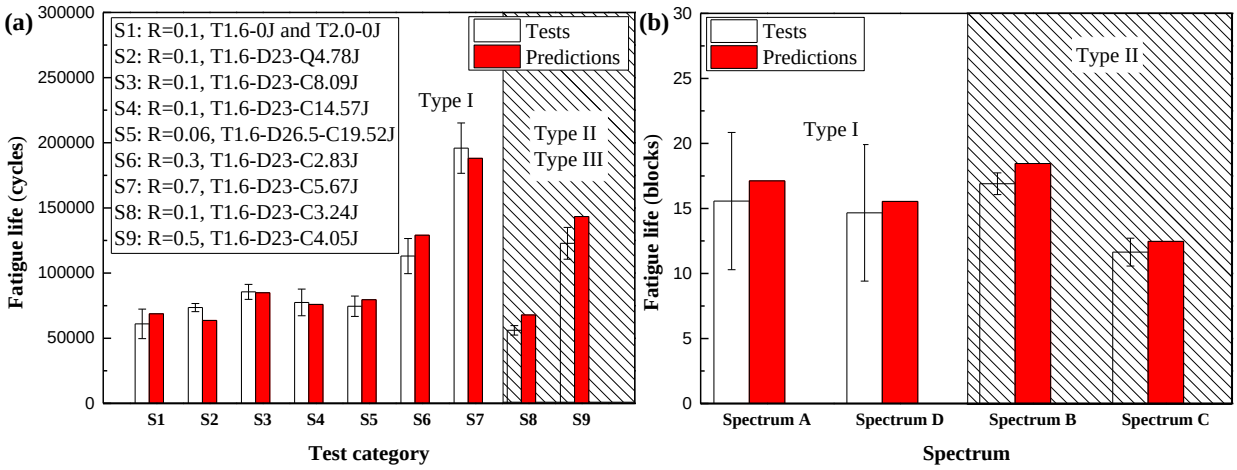


**Fig. 14** Comparison between predicted and experimental FCG life: (a) Constant amplitude FCG life; (b) Block spectrum loading FCG life (Note: Type I means crack through dent centre; Type II means crack across dent edge; Type III means crack bypassing the dent).

**Table 8** Input parameters used in predictions

| FCG at dent centre (mm/cycle) | | $m_0$ | | $\sigma_{max}$ (MPa) | $a_c$ (mm) | $r_{so}$ [17] |
|---|---|---|---|---|---|---|
| $\left(\frac{da}{dN}\right)_{test}$ | $\left[g\left(k_{tyy}\right)C\left(\Delta K-\Delta K_{th}\right)^{m_1}\left(1-R_{eff}\right)^{m_2}\right]_{calculate}$ | Calculations | Average | | | |
| 0.001034 | 0.009666 | 0.11 | 0.14 | 55 | 109.46 | 2.30 |
| 0.001838 | 0.009955 | 0.18 | | 62 | 105.04 | |
| 0.001316 | 0.009859 | 0.13 | | 74 | 98.27 | |

**Table 9** Crack growth increment $\Delta a_i$

| | |
|---|---|
| Crack growth increment | $\Delta a_i = \begin{cases} 1.77\times10^{-6} f\left(a_{i-1}\right) g\left(k_{\mathrm{tyy}}\left(a_{i-1}\right)\right)\left(\Delta K_i - 0.73\right)^{2.13}\left(1-R_{\mathrm{eff},i}\right)^{-0.97}, & \Delta K_i \geq 0.73 \\ 0, & \Delta K_i < 0.73 \end{cases}$ |
| Intermediate variables | $R_{\mathrm{eff}} = 1 - \dfrac{\Delta K}{\left(K_{\max}\right)_{\mathrm{eff}}}$<br>$\left(K_{\max}\right)_{\mathrm{eff}} = K_{\max} - \dfrac{\left(K_{\max}\right)_{\mathrm{OL}} - \left(K_{\max}\right)_{\mathrm{th}}}{\left(2.30-1\right)\left(K_{\max}\right)_{\mathrm{OL}}}\left(\left(K_{\max}\right)_{\mathrm{OL}}\sqrt{1-\dfrac{\Delta a'}{Z_{\mathrm{OL}}}} - K_{\max}\right)$<br>$\left(K_{\max}\right)_{\mathrm{th}} = \dfrac{\Delta K_{\mathrm{th}}}{\left(1-R\right)}$<br>$Z_{\mathrm{OL}} = \dfrac{1}{2\pi}\left(\dfrac{\left(K_{\max}\right)_{\mathrm{OL}}}{\sigma_{\mathrm{ys}}}\right)^2$<br>$f\left(a\right) = \begin{cases} \dfrac{0.86}{r_{\mathrm{p}}^2}\left(a - a_{\mathrm{dent}}\right)^2 + 0.14, & \text{inner dented region} \\ 1, & \text{outer dented region} \end{cases}$<br>$g\left(k_{\mathrm{tyy}}\right) = \left[k_{\mathrm{tyy}}\left(a\right)\right]^{2.13} = \left[\dfrac{\sigma_{\mathrm{yy}}\left(a\right)}{\sigma_{\mathrm{nom}}\left(a\right)}\right]^{2.13}$ |

## 5 Conclusions

This paper develops a fatigue crack growth model considering the effects of load interaction and LVI damage. The constant amplitude and block spectrum loading FCG tests of 7075-T62 aluminium-alloy thin-sheets are implemented to validate the effectiveness of the model. From the predictions and experiments, the following conclusions can be drawn from this study:

**(1)** The macroscopic FCG topologies of the post-impact specimens contains three types: crack through dent centre (Type I crack), crack across dent edge (Type II crack) and crack bypassing the dent (Type III crack). The crack tends to pass through the dent centre when the plastic zone associated with the dent is relatively large, as the Type I crack. In other cases, the crack would deflect around the dent region, as the Type II and III cracks.

**(2)** There are two competing mechanisms for the effect of LVI damage on the FCG rate of the post-impact aluminium-alloy thin-sheets. One is the retardation effect of the dented plastic zone caused by LVI, and the other is the acceleration effect of stress concentration due to impact-induced geometric changes. The retardation effect is dominant on the post-impact specimens with Type I crack, prolonging the FCG life of aluminium-alloy thin-sheets, but the acceleration effect is dominant on the post-impact specimens with Type II and Type III cracks, shortening the FCG life of aluminium-alloy thin-sheets.

**(3)** The proposed FCG model considering the effects of load interaction and LVI damage has been used to predict the FCG history and life of post-impact aluminium-alloy thin-sheets for all crack propagation types. A good correlation is achieved between predictions and experiments, demonstrating the practical and effective use of the developed models.


## Acknowledgements

This project was supported by the National Natural Science Foundation of China (Grant No. 51875021) and the China Scholarship Council. W. Tan acknowledges the financial support from EPSRC under grant EP/V049259/1.


## Appendix A

Taking the logarithm form of the Eq. (1) gives

$$\lg\left(\frac{da}{dN}\right)=\lg C+m_1\cdot\lg\left(\Delta K-\Delta K_{\text{th}}\right)+m_2\cdot\lg\left(1-R\right) \tag{A1}$$

setting $\lg\left(\frac{da}{dN}\right)=y$, $\lg C=b_0$, $m_1=b_1$, $\lg\left(\Delta K-\Delta K_{\text{th}}\right)=x_1$, $m_2=b_2$ and $\lg\left(1-R\right)=x_2$, then the form of the Eq. (A1) can be written as

$$y=b_0+b_1x_1+b_2x_2 \tag{A2}$$

According to the maximum likelihood principle, one has

$$\begin{cases} b_0=\overline{y}-b_1\overline{x}_1-b_2\overline{x}_2 \\ b_1=\dfrac{L_{12}L_{20}-L_{22}L_{10}}{L_{12}L_{21}-L_{11}L_{22}} \\ b_2=\dfrac{L_{21}L_{10}-L_{11}L_{20}}{L_{12}L_{21}-L_{11}L_{22}} \\ Q\left(\Delta K_{\text{th}}\right)=\sum_{i=1}^{l}\left(y_i-b_0-b_1x_1-b_2x_2\right)^2 \end{cases} \tag{A3}$$

with

$$
\begin{cases}
\overline{y} = \dfrac{1}{l}\sum_{i=1}^{l} y_i \\
\overline{x}_1 = \dfrac{1}{l}\sum_{i=1}^{l} x_{1i} \\
\overline{x}_2 = \dfrac{1}{l}\sum_{i=1}^{l} x_{2i} \\
L_{11} = \sum_{i=1}^{l}\left(x_{1i} - \overline{x}_1\right)^2 \\
L_{22} = \sum_{i=1}^{l}\left(x_{2i} - \overline{x}_2\right)^2 \\
L_{12} = L_{21} = \sum_{i=1}^{l}\left(x_{1i} - \overline{x}_1\right)\left(x_{2i} - \overline{x}_2\right) \\
L_{10} = \sum_{i=1}^{l}\left(x_{1i} - \overline{x}_1\right)\left(y_i - \overline{y}\right) \\
L_{20} = \sum_{i=1}^{l}\left(x_{2i} - \overline{x}_2\right)\left(y_i - \overline{y}\right)
\end{cases}
\tag{A4}
$$

It can be seen that $x_1$ is the function of undetermined constant $\Delta K_{\text{th}}$, so the parameters $\overline{x}_1$, $L_{11}$, $L_{12}$, $L_{10}$ and $Q$ are also the functions with regard to $\Delta K_{\text{th}}$. By means of the minimum value principle of $Q$, we can get

$$
\frac{\partial Q\left(\Delta K_{\text{th}}\right)}{\partial \Delta K_{\text{th}}} = 0 \tag{A5}
$$

By numerically solving Eq. (A5), the solution of $\Delta K_{\text{th}}$ can be obtained and the unknown model constants $C$, $m_1$ and $m_2$ are then determined as

$$
\begin{cases}
C = 10^{\left(\overline{y} - b_1\overline{x}_1 - b_2\overline{x}_2\right)} \\
m_1 = \dfrac{L_{12}L_{20} - L_{22}L_{10}}{L_{12}L_{21} - L_{11}L_{22}} \\
m_2 = \dfrac{L_{21}L_{10} - L_{11}L_{20}}{L_{12}L_{21} - L_{11}L_{22}}
\end{cases}
\tag{A6}
$$

## Appendix B

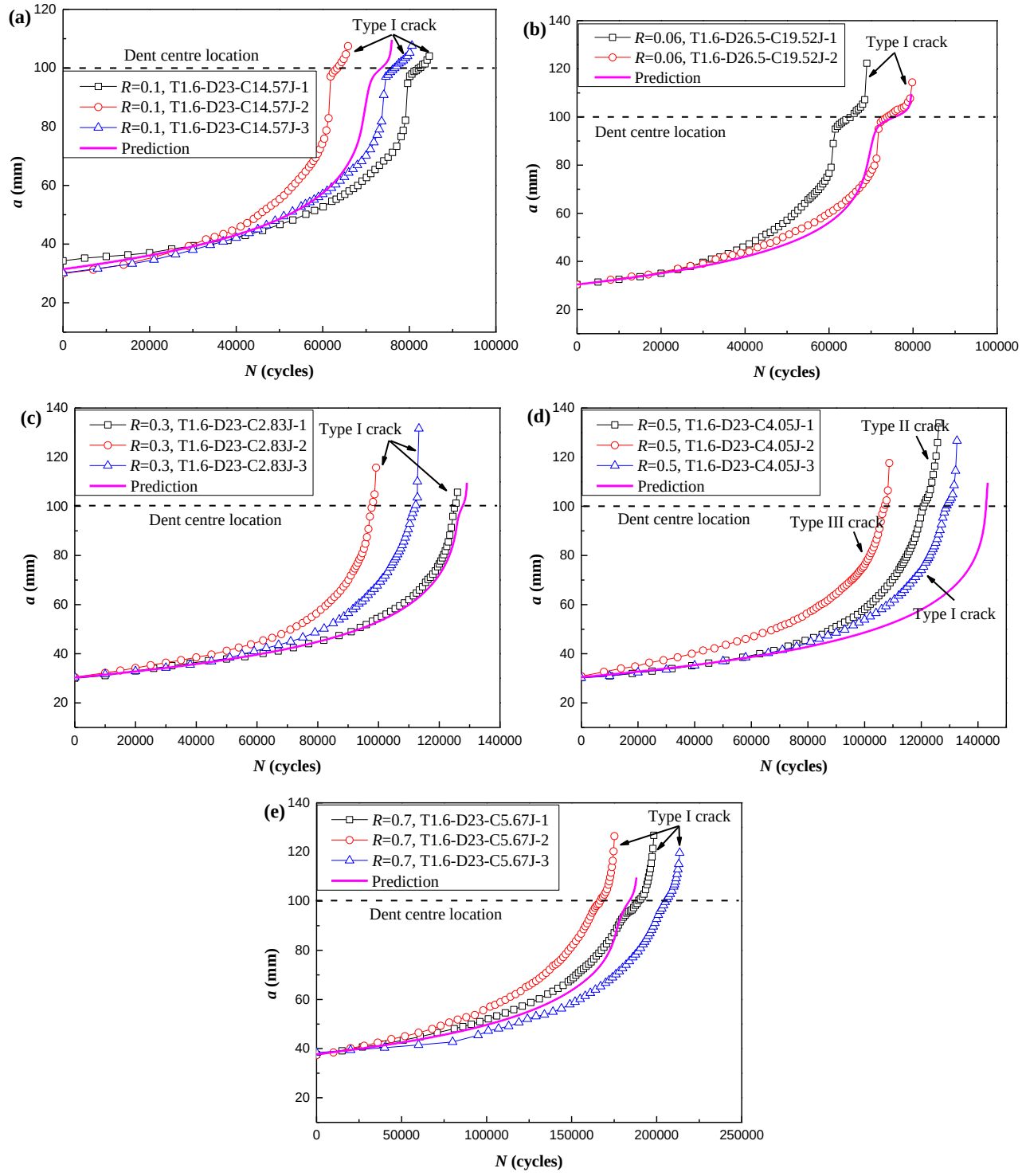


**Fig. B1** Comparison between predicted and experimental constant amplitude FCG *a*-*N* test data: (a) T1.6-D23-C14.57J specimens at $R$=0.1; (b) T1.6-D26.5-C19.52J specimens at $R$=0.06; (c) T1.6-D23-C2.83J specimens at $R$=0.3; (d) T1.6-D23-C4.05J specimens at $R$=0.5; (e) T1.6-D23-C5.67J specimens at $R$=0.7.

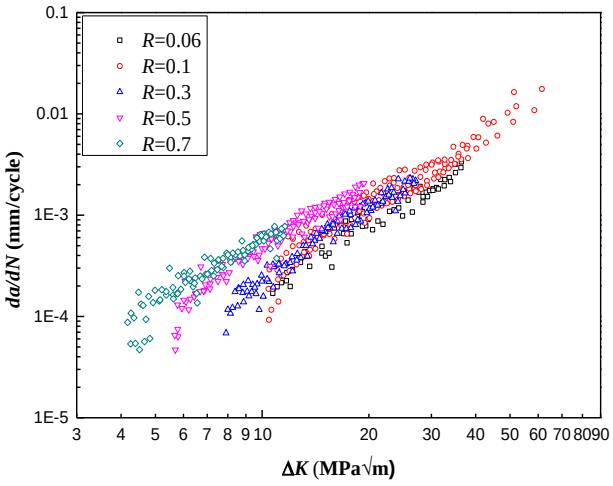


**Fig. B2** Constant amplitude FCG $da/dN$-$\Delta K$ test data.

## References

[1] Zhang X, Chan B, Lama S, Satikumar V, Shi S, Bao R. Influence of impact dents on the fatigue strength of aluminium alloy friction stir welds. Procedia Engineering, 2010, 2(1):1691-1700.

[2] Chen D, Cheng ZQ, Cunningham PR, Xiong JJ. Fatigue life prediction of 2524-T3 and 7075-T62 thin-sheet aluminium alloy with an initial impact dent under block spectrum loading. Fatigue & Fracture of Engineering Materials & Structures, 2021, 44:1096-1113.

[3] Xiong JJ, Shenoi RA. General aspects on structural integrity. Chinese Journal of Aeronautics, 2019, 32(1):114-132.

[4] Li ZG, Zhang DN, Peng CL, Ma CS, Zhang JH, Hu ZM, Zhang JZ, Zhao YN. The effect of local dents on the residual ultimate strength of 2024-T3 aluminium alloy plate used in aircraft under axial tension tests. Engineering Failure Analysis, 2015, 48:21-29.

[5] Li ZG, Zhang MY, Liu F, Ma CS, Zhang JH, Hu ZM, Zhang JZ, Zhao YN. Experimental study on the influence of dent on the residual ultimate strength of 2024-T3 aluminium alloy plate under axial compression. Transaction of Nonferrous Metals Society of China, 2014, 24:3084-3094.

[6] Lang NC, Kwon YW. Investigation of the effect of metallic fuselage dents on compressive failure loads. Journal of Aircraft, 2007, 44(6):2026-2033.

[7] Simmons F, Veciana J, Wallace J. Effects of dent removal on the design properties of fuselage skin material, American Institute of Aeronautics and Astronautics, 2000, AIAA 2000-1467.

[8] Li ZG, Feng RX, Wang Y, Wang LS. Experimental study on the effect of dents induced by impact on the fatigue life of 2024-T3 aluminium alloy plate. Engineering Structures, 2017, 137: 236-244.

[9] Chen YJ, Ji CM, Zhang CT, Wang FS, Song XX. Analysis for post-impact tensile-tensile fatigue damage of 2024-T3 sheets based on tests, digital image correlation (DIC) technique and finite element simulation. International Journal of Fatigue, 2019, 122(5):125-140.

[10] Chen YJ, Pan XC, Zhang CT, Cui ZF, Ji CM. Influence of foreign object impact mode on fatigue

performance of 2198-T8 Al-Li alloy thin sheets for fuselage. Fatigue & Fracture of Engineering Materials & Structures, 2021, 44:115-128.
[11] Ji CM, Chen YJ, Yang JC, Wang B, Sun YG. Dent-repaired fatigue performance and life prediction of thin sheet specimens under coupled multi-stage damage with impact and pre-fatigue. International Journal of Fatigue, 2021,146: 106148.
[12] Guijt C, Hill D, Rausch J, Fawaz S. The effect of dents in fuselage structures on fatigue and static stability. In: International committee on aeronautical fatigue (ICAF) conference, Hamburg, Germany, 2005.
[13] Shivalli P. The effect of dents on fatigue life and fatigue crack growth of aluminium 2024-T3 bare sheet. Wichita State University, 2006.
[14] Smith BL, Shivally P, Kumar B. Effect of dents on crack growth in aluminium alloy under constant-amplitude loading. Journal of Aircraft, 2012, 49(2):357-366.
[15] Wang CQ, Xiong JJ, Shenoi R A, Liu MD, Liu JZ. A modified model to depict corrosion fatigue crack growth behaviour for evaluating residual life of aluminium alloys. International Journal of Fatigue, 2016, 83(2):280-287.
[16] Willenborg J, Engle RM, Wood HA. A crack growth retardation model using an effective stress intensity concept. AFFDL, TM-71-1-FBR, 1971.
[17] Chang JB, Szamossi M, Liu KW. Random spectrum fatigue crack life predictions with or without considering load interactions. In: Chang JB, Hudson CM, editors. Methods and models for predicting fatigue crack growth under random loading, ASTM STP 748. Philadelphia: American Society for Testing and Materials; 1981, 115-132.
[18] Wheeler OE. Spectrum Loading and Crack Growth. Journal of Basic Engineering, 1972, 94(1):181-186.
[19] ASTM D7136/D7136M-15. Standard test method for measuring the damage resistance of a fiber-reinforced polymer matrix composite to a drop-weight impact event. American Society for Testing and Materials, 2015.
[20] Schwalbe KH, Setz W. R curve and fracture toughness of thin sheet materials. Journal of Testing and Evaluation, 1981, 9(4): 182-194.
[21] ASTM E647-15. Standard test method for measurement of fatigue crack growth rates. American Society for Testing and Materials, 2015.
[22] Zhao T, Zhang J, Jiang Y. A study of fatigue crack growth of 7075-T651 aluminium alloy. International Journal of Fatigue, 2008, 30(7): 1169-1180.
[23] Johnson GR, Cook WH. Fracture characteristics of three metals subjected to various strain, strain rate, temperatures and pressures. Engineering Fracture Mechanics, 1985;21(1):31-48.

[24] Børvik T, Hopperstad OS, Berstad T, Langseth M. Perforation of 12 mm thick steel plates by 20 mm diameter projectiles with flat, hemispherical and conical noses: part II: numerical simulations. International Journal of Impact Engineering, 2002, 27(1):37-64.
[25] Oscar J, Centeno G. Finite element modelling of rubber bushing for crash simulation-experimental tests and validation. Lund University, 2009.